nanomaterials

MDPI

Article

$MoTe_2$ Field-Effect Transistors with Low Contact Resistance through Phase Tuning by Laser Irradiation

Geun Yeol Bae [1,†], Jinsung Kim [2,†], Junyoung Kim [3,†], Siyoung Lee [2] and Eunho Lee [4,*]

1 Green and Sustainable Materials R&D Development, Korea Institute of Industrial Technology (KITECH), Cheonan 31056, Korea; gybae@kitech.re.kr
2 Department of Chemical Engineering, Pohang University of Science and Technology (POSTECH), Pohang 37673, Korea; jinsungkim@postech.ac.kr (J.K.); challenge@postech.ac.kr (S.L.)
3 Inspection Business Unit (IBU), Onto Innovation, Bloomington, MN 55435, USA; narsia89@gmail.com
4 Department of Chemical Engineering, Kumoh National Institute of Technology (KIT), Gumi 39177, Korea
* Correspondence: leeeh@kumoh.ac.kr
† Contributed equally.

Abstract: Due to their extraordinary electrical and physical properties, two-dimensional (2D) transition metal dichalcogenides (TMDs) are considered promising for use in next-generation electrical devices. However, the application of TMD-based devices is limited because of the Schottky barrier interface resulting from the absence of dangling bonds on the TMDs' surface. Here, we introduce a facile phase-tuning approach for forming a homogenous interface between semiconducting hexagonal (2H) and semi-metallic monoclinic (1T′) molybdenum ditelluride ($MoTe_2$). The formation of ohmic contacts increases the charge carrier mobility of $MoTe_2$ field-effect transistor devices to 16.1 $cm^2\ V^{-1}s^{-1}$ with high reproducibility, while maintaining a high on/off current ratio by efficiently improving charge injection at the interface. The proposed method enables a simple fabrication process, local patterning, and large-area scaling for the creation of high-performance 2D electronic devices.

Keywords: transition metal dichalcogenides; 2D materials; chemical vapor deposition; phase; contact resistance

Citation: Bae, G.Y.; Kim, J.; Kim, J.; Lee, S.; Lee, E. $MoTe_2$ Field-Effect Transistors with Low Contact Resistance through Phase Tuning by Laser Irradiation. *Nanomaterials* **2021**, *11*, 2805. https://doi.org/10.3390/nano11112805

Academic Editors: Filippo Giannazzo and Ivan Shtepliuk

Received: 27 September 2021
Accepted: 20 October 2021
Published: 22 October 2021

1. Introduction

Two-dimensional (2D) materials have received much attention owing to their unique physical, chemical, and electronic properties [1–5]. In particular, hexagonal group-VI 2D transition metal dichalcogenides (TMDs) have received significant research interest due to their exotic bandgap opening and strong spin-orbit coupling, which shows their feasibility in various applications, such as logic transistors, memristor, piezoelectronics, spintronics, wearable/flexible devices, sensors, and valley optoelectronics, among many others [6–11]. Distorted octahedral (T) phase TMDs have recently received attention in the field because of their promising features in novel electronic devices and topological field-effect transistors (FETs) based on quantum spin Hall effects [12]. Unlike the semiconducting (2H) phase, which has a relatively high bandgap opening (≥1 eV) and high structural and environmental stability, the semi-metallic (1T′) phase with a slight band overlap near the Fermi level is often found to be metastable [12–18]. When this phase is used in FETs, the semiconducting layer comprises a single layer or a few layers and has a covalently bonded lattice, where all charge carriers are confined in an atomically thin channel path, resulting in excellent gate tunability and a high on/off current ratio (I_{on}/I_{off}). Hence, it has significant potential in the optimal scaling of transistors for single-atom devices. However, only inhomogeneous centimeter-scale 1T′ MoS_2 has been reported [19]; this limits the size of the 1T′ TMD region for scalable applications. Thin-film tellurides, such as $MoTe_2$ and WTe_2, feature the most optimized electronic features, including superconductivity, quantum spin Hall state, and 2H, 1T, and 1T′ phases [12,20–25]. In particular, $MoTe_2$ is receiving broad

attention for phase-tunable memory devices owing to the small energy gap between the 2H and 1T′ phases, and strain-induced phase switching, gating, and heating have been experimentally demonstrated [26–30]. Despite increasing interest in tellurides, creating large-scale 1T′-phase $MoTe_2$ thin films in electronic applications remains a challenge, as does precisely controlling the number of layer depositions.

Creating an ohmic contact is another obstacle in developing high-performance ultrathin TMD devices because of the lack of surface dangling bonds and the high surface-to-volume ratio. To minimize the Schottky barrier between the semiconducting channel and metallic electrode, previous studies have focused on the contact interface, including the alignment of the work functions of Co, Sc, and Au/Ti electrodes with the conduction and valence band edges of the active layer [31–35]. Fermi-level pinning near the interface has been found to significantly affect device characteristics. In addition, the abundant metal electrodes near the conduction band were also found to improve device performance, owing to the effective carrier injection, which resulted in a decrease in the contact resistance [31]. For example, graphene-electrode-based FET devices show the advantages of electrical properties such as a tunable work function, high electrical conductivity, and nominal damage to the active layer. Transfer-free direct graphene synthesis on the MoS_2 layer resulted in a barrier height of 0 meV at a high gate voltage. Consequently, a high charge carrier mobility can be obtained due to the modified contact resistance and ohmic contact of the graphene and the MoS_2 layer [36]. The contact materials are suggested to form a highly conductive state for the active channel; this ensures a low interface resistance and facilitates carrier injection. However, doping mechanisms for nanoelectronics are typically not straightforward due to their limited doping levels, stability, and the complexity of the process [37]. Therefore, methods for obtaining two different electrical characteristics within a single element layer should be explored to fabricate high-performance electronic devices.

Here, we demonstrate a robust phase-tuning method that enables high-performance $MoTe_2$ FETs with a heterophase and homojunction interface. We developed a locally patterned semi-metallic 1T′ phase on ultrathin semiconducting $MoTe_2$ nanosheets by laser irradiation. Laser-irradiated 1T′ $MoTe_2$ FET devices exhibited enhanced electrical performances due to the effective charge injection via the homojunction interface. Additionally, we demonstrated a contact resistance of 93 kΩ·μm. This low contact resistance resulted from the work function of the 1T′ $MoTe_2$ and the 2H conduction band near the vacuum level. Furthermore, 1T′ $MoTe_2$ FET devices showed better overall performance than that of the semiconducting 2H $MoTe_2$ FETs. In addition, we measured the electrical properties in the atmosphere and obtained an average mobility of 16.1 $cm^2\ V^{-1}S^{-1}$, a high on/off ratio of more than 10^5, and a subthreshold swing of 98 mV dec^{-1} from 36 $MoTe_2$ FET devices. Laser-irradiation-assisted 2H–1T′ phase conversion is highly reproducible, suitable for scaling up and applying to large areas, and feasible for engineering the contact interfaces of 2D layered materials for atomically thin nanoelectronics in the near future.

2. Materials and Methods

The mixture of MoO_3/NaCl (4.0 mg/2.3 mg) for $MoTe_2$ synthesis was placed in a sample boat, and the target substrate (SiO_2/Si substrate) was placed at the top of the boat. A tellurium powder in a crucible for the tellurization of MoO_3 was placed upstream of the Ar carrier gas. After evacuation, the SiO_2/Si substrate was heated to T = 750 °C at a pressure of p = 350 Torr.

A p++ Si/SiO_2 300 nm wafer was used as a rigid substrate and gate electrode to fabricate the $MoTe_2$ FETs. Before fabricating the devices, the substrate was rinsed using ethanol, acetone, isopropyl alcohol, and deionized water. The device fabrication was completed by synthesizing a $MoTe_2$ active layer according to the method described above. To pattern S/D electrodes on the $MoTe_2$, the shadow mask, with various channel lengths from 30 to 200 μm, was aligned. Then, a Au (30 nm)/Ti (3 nm) electrode was deposited through the thermal evaporator. After fabrication of $MoTe_2$ FETs, the laser, having the

wavelength of 532 nm, was irradiated at the interface $MoTe_2$ and S/D electrodes to induce phase transition. The exposure time was varied from 1 to 8 s at an ambient atmosphere.

The crystalline properties of $MoTe_2$ were characterized via Raman spectroscopy (WITec Alpha 300R, Ulm, Germany), and its thickness was measured using atomic force microscopy (AFM; Bruker MultiMode 8, Camarillo, CA, USA). The chemical composition and bonding properties of $MoTe_2$ were determined using X-ray Photoelectron Spectroscopy (XPS, PHI VersaProbe, Chanhassen, MN, USA). The electrical characteristics were analyzed using a Keithley 2636A source meter (Tektronix, Beaverton, OR, USA) under an ambient atmosphere.

3. Results and Discussion

Figure 1a shows a schematic of the synthesis of monolayered $MoTe_2$ via chemical vapor deposition (CVD) on a SiO_2/Si substrate. Figure 1b and Figure S1. show the optical images of the obtained film. The material synthesis is described in detail in the Materials and Methods section. An AFM image and a height profile (Figure 1c) show the thickness and demonstrate that the $MoTe_2$ flakes on SiO_2/Si have a height of 0.87 nm, indicating that they form a monolayer. Figure 1d shows the Raman spectra of $MoTe_2$ on the SiO_2/Si substrate after laser irradiation from 1 to 8 s. Laser irradiation causes structural phase evolution in the exposed area. All $MoTe_2$ films exhibit a relatively weak peak at 235 cm^{-1} (in-plane E^1_{2g} mode) but a strong prominent peak at 159 cm^{-1} (out-of-plane A_g mode) under 532 nm laser excitation [38–40]. The E^1_{2g} mode signal is typically strong for 2D $MoTe_2$ flakes; however, the A_g mode signal was higher than that of the E^1_{2g} mode, indicating that the in-plane signal was diminished.

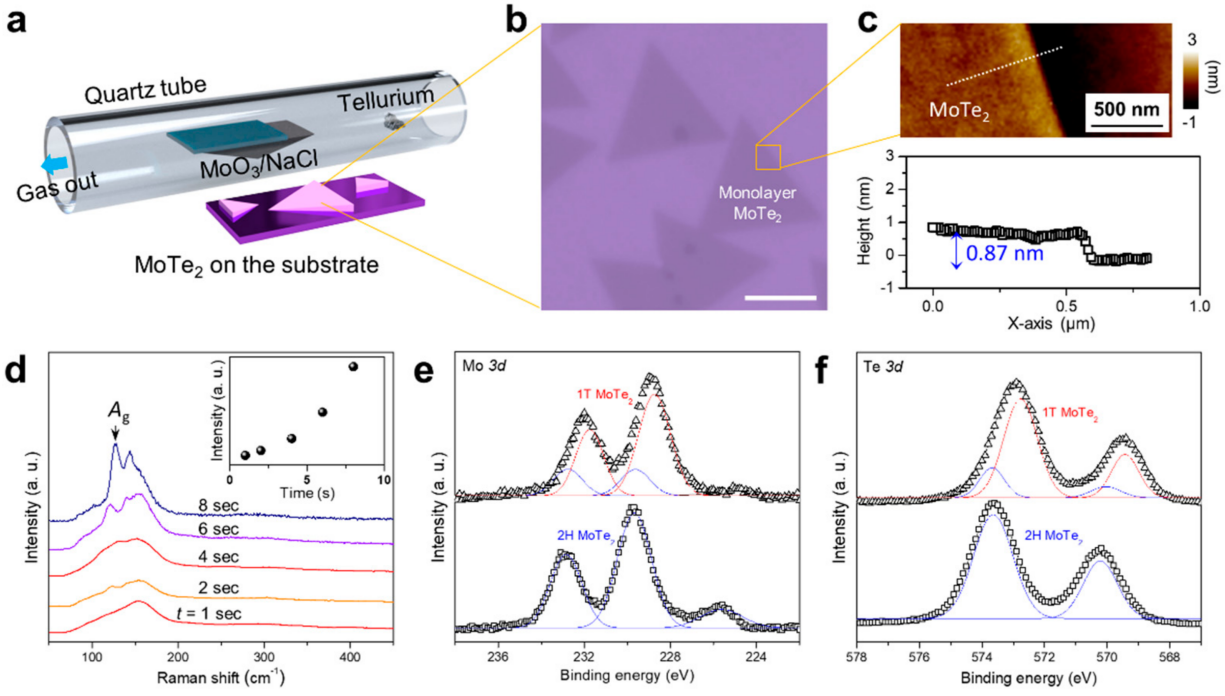

Figure 1. Characterization of CVD-grown $MoTe_2$: (**a**) Schematic of CVD synthesis of $MoTe_2$ on SiO_2/Si substrate using salt-assisted growth; (**b**) Optical microscopy image of triangular monolayered $MoTe_2$ nuclei on the SiO_2/Si substrate. The scale bar is 2 μm; (**c**) AFM image of $MoTe_2$ and the height profile corresponding to the white dashed line; the thickness of the $MoTe_2$ is 0.87 nm; (**d**) Raman spectra of $MoTe_2$ at various laser irradiation times. The inset shows the evolution of the Ag peak related to the 1T′ phase of $MoTe_2$ with time. XPS spectra show (**e**) Mo 3*d* and (**f**) Te 3*d* peaks of the 1T′ and 2H phases of $MoTe_2$.

To obtain the critical laser irradiation time for the phase transition in the $MoTe_2$ samples on the SiO_2/Si substrate, the desired area was gradually and carefully exposed to irradiation by a laser with a power of 2.6 mW and a wavelength of 532 nm. In addition, the Raman spectra were measured after laser irradiation for each duration. The evolution trend was similar for all cases. The E^1_{2g} peak intensity decreased gradually with increasing laser irradiation time, and when the laser irradiation time reached the critical value, two new peaks appeared at 127 and 141 cm^{-1}, which correspond to the A_g mode of 1T′ $MoTe_2$ [30]. These peaks provide direct evidence of the phase transition from the 2H phase to the 1T′ phase. The A_g intensity is plotted as a function of the irradiation time in the inset of Figure 1d. The critical laser irradiation time for the phase transition of $MoTe_2$ from the 2H phase to the 1T′ phase was 8 s. The phase transition of $MoTe_2$ might be explained by the Te vacancy formation in $MoTe_2$, which results in alterations in the stoichiometry of Mo atoms; this leads to reconstruction of its atomic structure, and phase transition of the 2H phase to the 1T′ phase.

Figure 1e,f show the XPS spectra of Mo and Te, respectively. The spectra were obtained before and after laser irradiation for 8 s. As shown in Figure 1e, prominent peaks at 229.4 eV (Mo $3d_{5/2}$), 233.0 eV (Mo $3d_{3/2}$), 570.3 eV (Te $3d_{5/2}$), and 573.5 eV (Te $3d_{3/2}$) can be observed in the pristine sample, corresponding to the 2H phase. By contrast, the XPS peaks for 1T′ $MoTe_2$ can be observed at 229.0 eV (Mo $3d_{5/2}$), 232.2 eV (Mo $3d_{3/2}$), 569.6 eV (Te $3d_{5/2}$), and 572.9 eV (Te $3d_{3/2}$). The binding energies of Mo and Te atoms in the irradiated area exhibit an energy shift of 0.4–0.8 eV between two different phases on $MoTe_2$. This shift can be attributed to the distinct lattice symmetry of the 2H and 1T′ phases of $MoTe_2$ [41]. This value is similar to previously reported energy shift values ranging from 0.4 to 0.6 eV [41–43]. Moreover, we observed that in 1T′ $MoTe_2$, Te *3d* peaks are blue-shifted by 0.7 eV, whereas the Mo *3d* peaks are blue-shifted by 0.4 eV. It has also been previously reported that chalcogen deficiency in TMDs decreases the binding energy of the transition metal by approximately the same amount [44].

To evaluate the feasibility of $MoTe_2$ with a heterophase homojunction interface for electronic applications, $MoTe_2$ FET devices were fabricated on a SiO_2/Si substrate. Figure 2a,b show a schematic of the $MoTe_2$ FET device structure and its A_g Raman mapping image after laser irradiation, respectively. The A_g Raman mappings show that the $MoTe_2$ monolayer is not limited to deposit uniformly over the entire area but also includes the channel region, resulting in 2H to 1T′ phase-transformed $MoTe_2$ devices. Overall, the laser irradiation approach efficiently enabled the fabrication of $MoTe_2$ FETs by simple phase tuning. The transfer characteristics of back-gate FETs were investigated under laser irradiation. Figure 2c,d show the drain current (I_D) as a function of the gate voltage (V_G) of the 2H and 1T′ $MoTe_2$ FETs, respectively. The measured curves show a high on/off ratio of more than 10^5 and typical p-type transistor characteristics. From the obtained *I-V* curves of the $MoTe_2$ FETs, we determined the field-effect mobility (μ) as follows:

$$I_D = \frac{W}{2L} Cu(V_{GS} - V_T)^2 \quad (1)$$

where I_D is the drain current, W is the channel width of the electrode, L is the channel length of the electrode, C is the area capacitance of the SiO_2 layer, V_{GS} is the gate voltage, and V_T is the threshold voltage. At the saturation regime, the average mobility values of 13.6 $cm^2\ V^{-1}s^{-1}$ for the 36 2H-phase devices and 16.1 $cm^2\ V^{-1}s^{-1}$ for the 36 1T′-phase devices were obtained, respectively; these values represent an increase of nearly 20% (Figure 2e). The high on/off ratios for the 36 2H $MoTe_2$ FETs devices were well preserved after phase tuning to 1T′ by laser irradiation, as shown in Figure 2f. Moreover, 1T′ phase transformed FETs showed a high on-current level (~3.1 mA), and threshold voltage. This indicates that charge carrier movements were well preserved or improved after forming the homojunction interface. Interestingly, according to the statistical results, the on-current, as well as the off-current, slightly increased, so the carrier mobility of the 1T′ $MoTe_2$ FETs was increased overall, but the average on/off ratio decreased. These results demonstrate that

the heterophase homojunction interface between the active layer and electrodes enhanced the electrical performance of the $MoTe_2$ FET devices and indicates the feasibility of the laser irradiation approach.

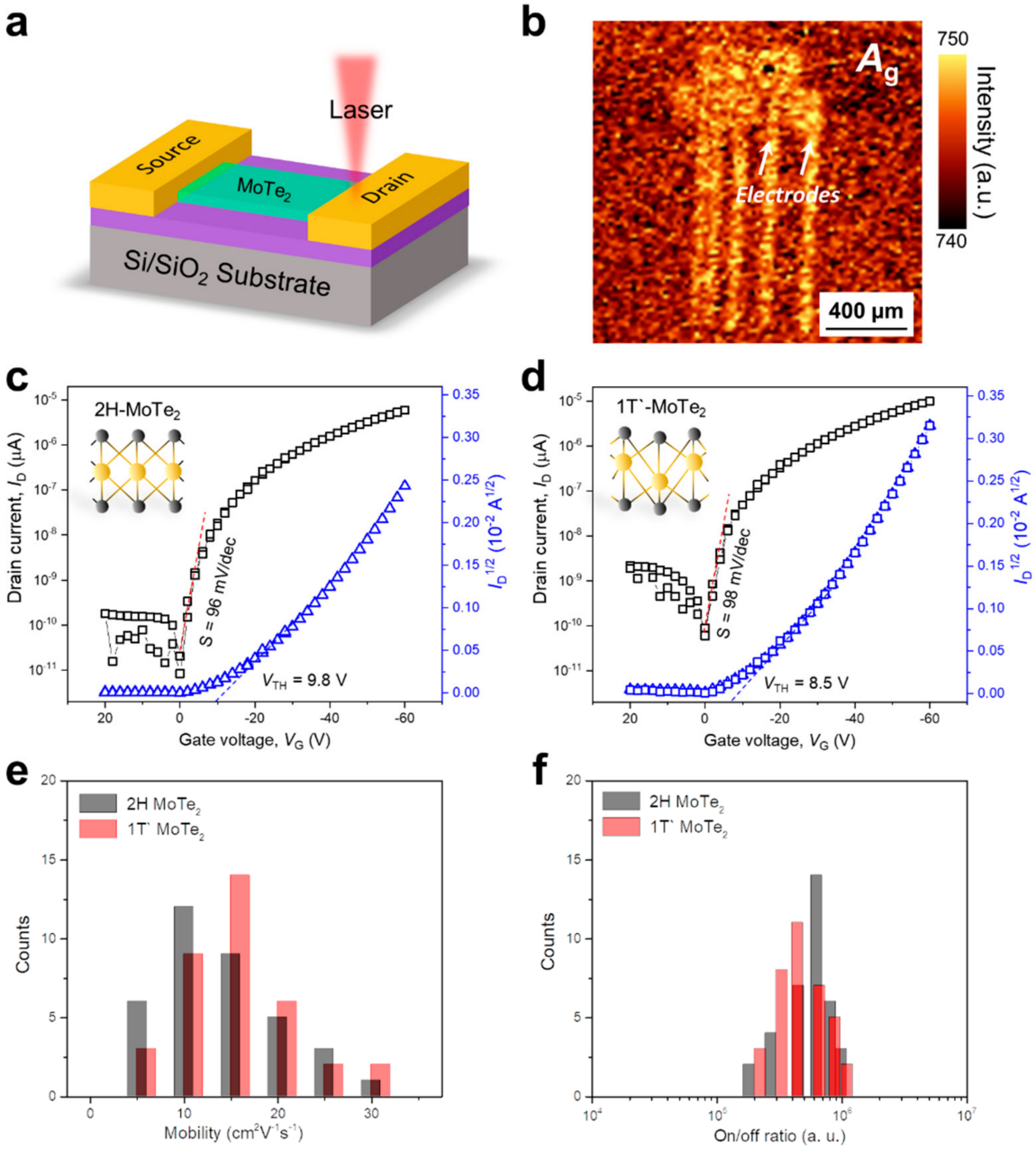

Figure 2. Electrical characterization of 2H and 1T′-phase of $MoTe_2$ FETs: (**a**) Schematic structure of $MoTe_2$ FETs on SiO_2/Si substrate; the dimensions of the $MoTe_2$ FETs are the following: channel length 20 μm and width 400 μm. (**b**) Two-dimensional A_g Raman mapping image of $MoTe_2$ FETs on SiO_2/Si substrate after laser irradiation. Transfer curves of (**c**) 2H $MoTe_2$ and (**d**) 1T′ $MoTe_2$ FETs after laser irradiation; (**e**) Statistical diagram of the measured carrier mobilities; (**f**) On/off ratio of the 36 fabricated 2H and 1T′ FETs.

The contact resistances were obtained via the transfer length method (TLM) to demonstrate the reasons for the improvement in the electrical characteristics. From the TLM plots, the contact resistance values were extracted from the value for a channel length of zero. To obtain an excellent statistical agreement, at least 36 samples were measured and analyzed. Figure 3a,b show that the resistance of 1T′ $MoTe_2$ decreased by 22.5%, from 120 to 93 kΩ·μm. Many studies have reported that the interface characteristics are among the

main factors affecting contact resistance [45,46]. In the 1T′ $MoTe_2$ device, phase tuning by laser irradiation helps reduce the contact resistance between the semiconducting layer and the electrodes. This increases the mobility and decreases the threshold voltage by reducing the contact resistance. Figure 3c shows that the 2H $MoTe_2$ device exhibits nonlinear I_D–V_{DS} characteristics, indicating Schottky behavior, whereas an ohmic-like behavior is observed in the 1T′ $MoTe_2$ device performance, as shown in Figure 3d.

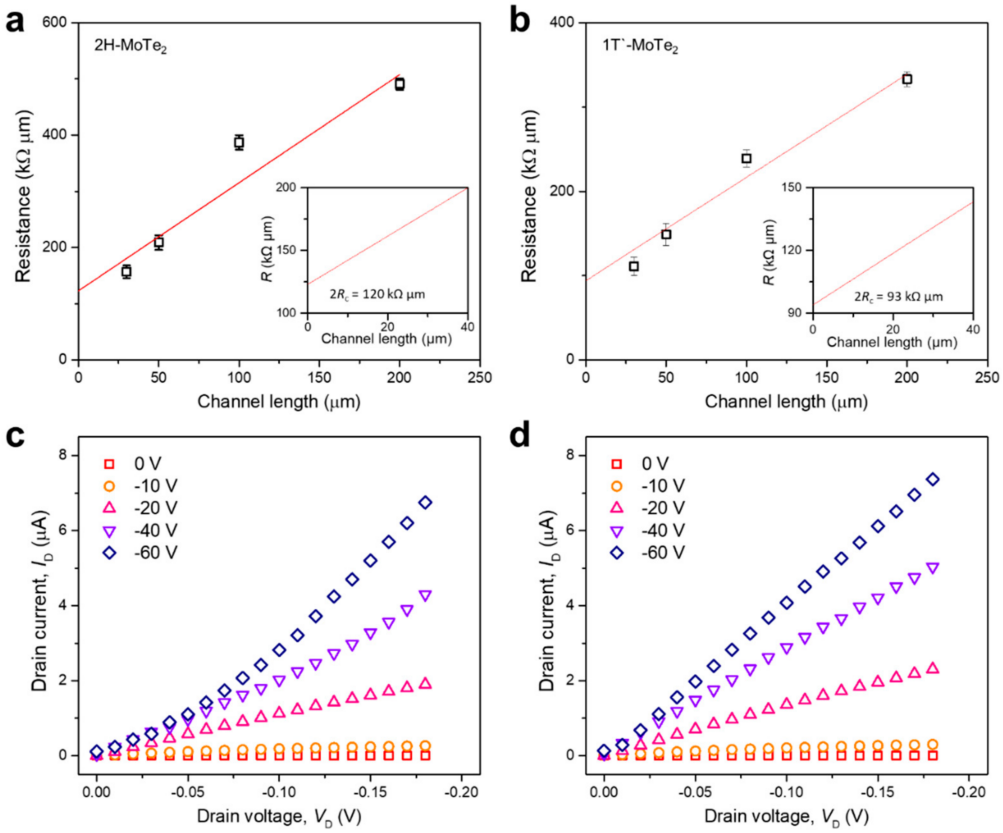

Figure 3. Contact resistance of the 2H-phase and 1T′-phase of $MoTe_2$ FETs: (**a**) 2H $MoTe_2$ and (**b**) 1T′ $MoTe_2$ FETs after laser irradiation. The channel width is normalized using the resistance obtained from 2H $MoTe_2$ FETs; Output curves of (**c**) 2H and (**d**) 1T′-phase $MoTe_2$ FETs after laser irradiation; the FETs have gate voltages ranging from 0 to −60 V.

To further quantify the ohmic contact in these devices, the barrier height at the interface between the S/D electrodes and the $MoTe_2$ channel was studied [36,47]. The electrical properties were characterized at various temperatures to measure the energy levels of the metallic and semiconducting layers in the 1T′-phase $MoTe_2$ devices, as shown in Figure 4.

As the temperature increases, the drain current (I_D) also increases due to the hopping transport, which dominates the charge transport in $MoTe_2$ [48]. The increase in the current with temperature is due to the increased charge carriers at elevated temperatures, where the thermal energy is sufficient to overcome the activation energy. The results were fitted using the following thermal emission equation to obtain an Arrhenius plot of the laser-irradiated 1T′ $MoTe_2$ devices at different gate voltages:

$$I_{DS} = AT^{3/2} \exp\left(-\frac{q\varphi_B}{k_B T}\right)\left[\exp\left(\frac{qV_{DS}}{nk_B T}\right) - 1\right] \quad (2)$$

where I_{DS} is current, A is the Richardson's constant, T is the temperature, φ_B is the Schottky barrier, q is the charge constant, k_B is the Boltzmann constant, V_{DS} is the drain voltage, and n is the nonideal factor [32,49]. When $V_{DS} >> k_B T$, Equation (2) can be simplified as:

$$ln\left(\frac{I_{DS}}{T^{3/2}}\right) = -\frac{q\left(\varphi_B - \frac{V_{DS}}{n}\right)}{k_B T} + \ln(A) \quad (3)$$

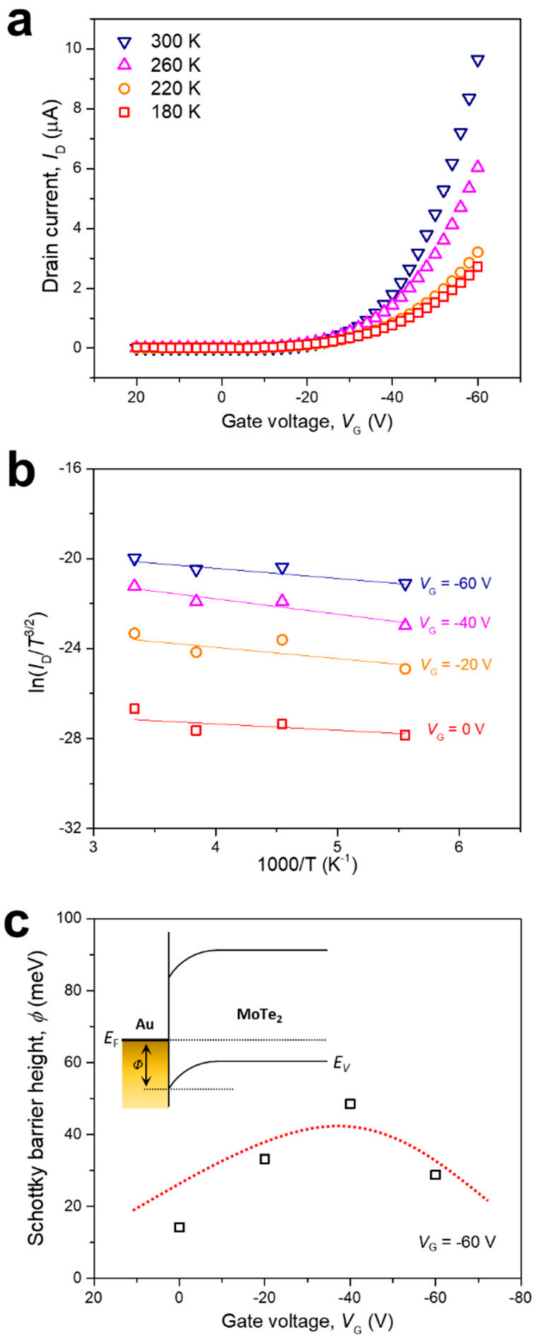

Figure 4. Transfer curves and Schottky barrier of 1T′ $MoTe_2$ FETs at various temperatures: (**a**) Transfer curves obtained from laser-irradiated 1T′ $MoTe_2$ FETs at temperatures ranging from 180 to 300 K; (**b**) Arrhenius plot of laser-irradiated 1T′ $MoTe_2$ FETs with gate voltages ranging from 0 V to −60 V; (**c**) Schottky barrier height of laser-irradiated 1T′ $MoTe_2$ FETs. The inset shows the schematic of the Schottky barrier of *p*-type $MoTe_2$ with contact to the Au electrode.

The Schottky energy barrier (φ_B) can be expressed as the slope of the simplified equation in a curve of $\ln(I_{DS}/T^{3/2})$ versus 1000/T. The results were plotted at different V_G values for the 1T′ $MoTe_2$ FETs (Figure 4b). Finally, to obtain the nonideal factor (n), which is required to calculate φ_B for each slope, we used the following equation:

$$\frac{dV_{DS}}{dI_{DS}} = \frac{nk_BT}{q}\frac{1}{I_{DS}} + R_s \quad (4)$$

where R_s is the series resistance. We calculated n as the slope of a curve of dV_{DS}/dI_{DS} versus $1/I_{DS}$ and obtained a value of 9.93 (Figure S2) [36,49]. The value of φ_B was calculated from these results (Figure 4c). When a zero-gate voltage was applied, the Schottky energy barrier was lower in the 1T′ $MoTe_2$ device than in the 2H $MoTe_2$ device, demonstrating that 1T′ $MoTe_2$ forms a sharper interface between the electrode and the semiconducting layer than 2H $MoTe_2$ (Figure S3). Note that the difference in transistor polarity between the 2H and 1T′ devices is explained simply by modifying the Schottky barrier height by laser irradiation. An advantage of the 1T′ device is that the S/D electrodes are side contacts rather than vertical contacts, providing better device properties [50,51]. Furthermore, this result is fundamentally different from previously reported results on chemical doping. The transistor polarity change mechanism preserves the electron and hole mobilities. It efficiently improves electron mobility with a facile approach. Moreover, 1T′-phase devices are highly independent of the metal of the S/D electrodes. We designed 1T′ $MoTe_2$ devices with the same electrodes and achieved a yield of nearly 100% with consistent performance. Additionally, an ohmic-like contact was achieved at the interface between the active layer and electrodes, which improved the charge carrier injection without barriers. Although the 1T′ phase is metastable, it has been demonstrated that stability can be maintained under environmental conditions after facile laser irradiation.

4. Conclusions

In summary, we developed a facile method for phase tuning from 2H to 1T′ $MoTe_2$ by laser irradiation. This method produces a 1T′ $MoTe_2$ monolayer that facilitates charge injection at the interface and thus improves the electrical characteristics of the $MoTe_2$ FETs. Moreover, we showed that phase tunability could help effectively reduce the contact resistance at the interface between the S/D electrodes and the $MoTe_2$ channel, thus providing high carrier mobility of the FETs. Additionally, we demonstrated that the 1T′ phase of $MoTe_2$ is a heterophase homojunction electrode with a low contact resistance value of 93 kΩ·μm at zero gate bias. The low contact resistance results in a high on-current of 3.1 $mA^{1/2}$, and a high charge carrier mobility of 16.1 $cm^2\ V^{-1}s^{-1}$. Our work demonstrates that phase engineering is a practical approach for improving the performance of $MoTe_2$ devices.

Supplementary Materials: The following are available online at https://www.mdpi.com/article/10.3390/nano11112805/s1, Figure S1: Optical image of the CVD-grown $MoTe_2$ on the SiO_2/Si substrate, Figure S2: I-V curve of $MoTe_2$ FETs, Figure S3: Schottky barrier height of $MoTe_2$ FETs. Table S1. Comparison the device performances.

Author Contributions: Conceptualization, J.K. (Junyoung Kim) and E.L.; methodology, G.Y.B.; software, E.L.; validation, G.Y.B., J.K. (Jinsung Kim) and S.L.; formal analysis, J.K. (Junyoung Kim); investigation, G.Y.B. and J.K. (Jinsung Kim); resources, J.K. (Junyoung Kim); data curation, J.K. (Junyoung Kim) and S.L.; writing—original draft preparation, J.K. (Junyoung Kim) and E.L.; writing—review and editing, J.K. (Junyoung Kim) and E.L.; visualization, E.L.; supervision, E.L.; project administration, E.L.; funding acquisition, E.L.; contributed equally, G.Y.B., J.K. (Jinsung Kim) and J.K. (Junyoung Kim). All authors have read and agreed to the published version of the manuscript.

Funding: This research was funded by National Research Foundation of Korea (NRF) grant funded by the Korean government (MSIT) (No. 2021R1G1A1093058).

Data Availability Statement: Not applicable.

Acknowledgments: The authors acknowledge the illustration support from Noah Studio LLC, Dallas, TX, USA.

Conflicts of Interest: The authors declare no conflict of interest.

References

1. Radisavljevic, B.; Radenovic, A.; Brivio, J.; Giacometti, V.; Kis, A. Single-layer MoS_2 transistors. *Nat. Nanotechnol.* **2011**, *6*, 147–150. [CrossRef]
2. Zhang, Z.; Chen, P.; Duan, X.; Zang, K.; Luo, J.; Duan, X. Robust epitaxial growth of two-dimensional heterostructures, multiheterostructures, and superlattices. *Science* **2017**, *357*, 788–792. [CrossRef]
3. Li, X.; Cai, W.; An, J.; Kim, S.; Nah, J.; Yang, D.; Piner, R.; Velamakanni, A.; Jung, I.; Tutuc, E.; et al. Large-Area Synthesis of High-Quality and Uniform Graphene Films on Copper Foils. *Science* **2009**, *324*, 1312–1314. [CrossRef]
4. Pradhan, N.R.; Rhodes, D.; Feng, S.; Xin, Y.; Memaran, S.; Moon, B.-H.; Terrones, H.; Terrones, M.; Balicas, L. Field-Effect Transistors Based on Few-Layered α-$MoTe_2$. *ACS Nano* **2014**, *8*, 5911–5920. [CrossRef] [PubMed]
5. Shen, D.W.; Xie, B.P.; Zhao, J.F.; Yang, L.X.; Fang, L.; Shi, J.; He, R.H.; Lu, D.H.; Wen, H.H.; Feng, D.L. Novel Mechanism of a Charge Density Wave in a Transition Metal Dichalcogenide. *Phys. Rev. Lett.* **2007**, *99*, 216404. [CrossRef] [PubMed]
6. Zhang, Y.J.; Oka, T.; Suzuki, R.; Ye, J.T.; Iwasa, Y. Electrically Switchable Chiral Light-Emitting Transistor. *Science* **2014**, *344*, 725–728. [CrossRef] [PubMed]
7. Choi, W.; Kim, J.; Lee, E.; Mehta, G.; Prasad, V. Asymmetric 2D MoS_2 for Scalable and High-Performance Piezoelectric Sensors. *ACS Appl. Mater. Interfaces* **2021**, *13*, 13596–13603. [CrossRef] [PubMed]
8. Lee, E.; Kim, J.; An, T.K. Direct growth of CVD graphene on 3D-architectured substrates for highly stable tactile sensors. *Chin. J. Phys.* **2020**, *67*, 569–575. [CrossRef]
9. Kim, J.; Lee, E.; Mehta, G.; Choi, W. Stable and high-performance piezoelectric sensor via CVD grown WS_2. *Nanotechnology* **2020**, *31*, 445203. [CrossRef]
10. Lee, E.; Kim, J.; Bhoyate, S.; Cho, K.; Choi, W. Realizing Scalable Two-Dimensional MoS_2 Synaptic Devices for Neuromorphic Computing. *Chem. Mater.* **2020**, *32*, 10447–10455. [CrossRef]
11. Bhoyate, S.D.; Mhin, S.; Jeon, J.-E.; Park, K.; Kim, J.; Choi, W. Stable and High-Energy-Density Zn-Ion Rechargeable Batteries Based on a MoS_2-Coated Zn Anode. *ACS Appl. Mater. Interfaces* **2020**, *12*, 27249–27257. [CrossRef] [PubMed]
12. Qian, X.; Liu, J.; Fu, L.; Li, J. Quantum spin Hall effect in two-dimensional transition metal dichalcogenides. *Science* **2014**, *346*, 1344–1347. [CrossRef]
13. Chhowalla, M.; Shin, H.S.; Eda, G.; Li, L.-J.; Loh, K.; Zhang, H. The chemistry of two-dimensional layered transition metal dichalcogenide nanosheets. *Nat. Chem.* **2013**, *5*, 263–275. [CrossRef] [PubMed]
14. Vellinga, M.; de Jonge, R.; Haas, C. Semiconductor to metal transition in $MoTe_2$. *J. Solid State Chem.* **1970**, *2*, 299–302. [CrossRef]
15. Ali, M.N.; Xiong, J.; Flynn, S.; Tao, J.; Gibson, Q.D.; Schoop, L.; Liang, T.; Haldolaarachchige, N.; Hirschberger, M.; Ong, N.P.; et al. Large, non-saturating magnetoresistance in WTe_2. *Nature* **2014**, *514*, 205–208. [CrossRef] [PubMed]
16. Zandt, T.; Dwelk, H.; Janowitz, C.; Manzke, R. Quadratic temperature dependence up to 50 K of the resistivity of metallic $MoTe_2$. *J. Alloy. Compd.* **2007**, *442*, 216–218. [CrossRef]
17. Morgado, J.; Alcacer, L.; Henriques, R.; Lopes, E.B.; Almeida, M.; Fourmigué, M. Preparation and characterization of CPP_2I_3-δ single crystals. *Synth. Met.* **1993**, *56*, 1735–1740. [CrossRef]
18. Enyashin, A.N.; Yadgarov, L.; Houben, L.; Popov, I.; Weidenbach, M.; Tenne, R.; Bar Sadan, M.; Seifert, G. New Route for Stabilization of 1T-WS_2 and MoS_2 Phases. *J. Phys. Chem. C* **2011**, *115*, 24586–24591. [CrossRef]
19. Lin, Y.-C.; Dumcenco, D.O.; Huang, Y.-S.; Suenaga, K. Atomic mechanism of the semiconducting-to-metallic phase transition in single-layered MoS_2. *Nat. Nanotechnol.* **2014**, *9*, 391–396. [CrossRef]
20. Pan, X.-C.; Chen, X.; Liu, H.; Feng, Y.; Wei, Z.; Zhou, Y.; Chi, Z.; Pi, L.; Yen, F.; Song, F.; et al. Pressure-driven dome-shaped superconductivity and electronic structural evolution in tungsten ditelluride. *Nat. Commun.* **2015**, *6*, 7805. [CrossRef]
21. Kang, D.; Zhou, Y.; Yi, W.; Yang, C.; Guo, J.; Shi, Y.; Zhang, S.; Wang, Z.; Zhang, C.; Jiang, S.; et al. Superconductivity emerging from a suppressed large magnetoresistant state in tungsten ditelluride. *Nat. Commun.* **2015**, *6*, 7804. [CrossRef] [PubMed]
22. Qi, Y.; Naumov, P.; Ali, M.N.; Rajamathi, C.R.; Schnelle, W.; Barkalov, O.; Hanfland, M.; Wu, S.-C.; Shekhar, C.; Sun, Y.; et al. Superconductivity in Weyl semimetal candidate $MoTe_2$. *Nat. Commun.* **2016**, *7*, 11038. [CrossRef] [PubMed]
23. Wang, Z.; Gresch, D.; Soluyanov, A.; Xie, W.; Kushwaha, S.; Dai, X.; Troyer, M.; Cava, R.J.; Bernevig, B.A. $MoTe_2$: A Type-II Weyl Topological Metal. *Phys. Rev. Lett.* **2016**, *117*, 056805. [CrossRef] [PubMed]
24. Soluyanov, A.; Gresch, D.; Wang, Z.; Wu, Q.; Troyer, M.; Dai, X.; Bernevig, B.A. Type-II Weyl semimetals. *Nature* **2015**, *527*, 495–498. [CrossRef] [PubMed]
25. Wu, S.; Fatemi, V.; Gibson, Q.D.; Watanabe, K.; Taniguchi, T.; Cava, R.J.; Jarillo-Herrero, P. Observation of the quantum spin Hall effect up to 100 kelvin in a monolayer crystal. *Science* **2018**, *359*, 76–79. [CrossRef]
26. Xu, X.; Chen, S.; Liu, S.; Cheng, X.; Xu, W.; Li, P.; Wan, Y.; Yang, S.; Gong, W.; Yuan, K.; et al. Millimeter-Scale Single-Crystalline Semiconducting $MoTe_2$ via Solid-to-Solid Phase Transformation. *J. Am. Chem. Soc.* **2019**, *141*, 2128–2134. [CrossRef]
27. Hou, W.; Azizimanesh, A.; Sewaket, A.; Peña, T.; Watson, C.; Liu, M.; Askari, H.; Wu, S.M. Strain-based room-temperature non-volatile $MoTe_2$ ferroelectric phase change transistor. *Nat. Nanotechnol.* **2019**, *14*, 668–673. [CrossRef]
28. Wang, Y.; Xiao, J.; Zhu, H.; Li, Y.; Alsaid, Y.; Fong, K.Y.; Zhou, Y.; Wang, S.; Shi, W.; Wang, Y.; et al. Structural phase transition in monolayer $MoTe_2$ driven by electrostatic doping. *Nature* **2017**, *550*, 487–491. [CrossRef]

29. Zhang, C.; Kc, S.; Nie, Y.; Liang, C.; Vandenberghe, W.G.; Longo, R.C.; Zheng, Y.; Kong, F.; Hong, S.; Wallace, R.M.; et al. Charge Mediated Reversible Metal–Insulator Transition in Monolayer $MoTe_2$ and $W_xMo_{1-x}Te_2$ Alloy. *ACS Nano* **2016**, *10*, 7370–7375. [CrossRef]
30. Keum, D.H.; Cho, S.; Kim, J.H.; Choe, D.-H.; Sung, H.-J.; Kan, M.; Kang, H.; Hwang, J.-Y.; Kim, S.W.; Yang, H.; et al. Bandgap opening in few-layered monoclinic $MoTe_2$. *Nat. Phys.* **2015**, *11*, 482–486. [CrossRef]
31. Das, S.; Chen, H.-Y.; Penumatcha, A.V.; Appenzeller, J. High Performance Multilayer MoS_2 Transistors with Scandium Contacts. *Nano Lett.* **2012**, *13*, 100–105. [CrossRef]
32. Chen, J.-R.; Odenthal, P.M.; Swartz, A.G.; Floyd, G.C.; Wen, H.; Luo, K.Y.; Kawakami, R.K. Control of Schottky Barriers in Single Layer MoS_2 Transistors with Ferromagnetic Contacts. *Nano Lett.* **2013**, *13*, 3106–3110. [CrossRef]
33. Popov, I.Y.; Seifert, G.; Tománek, D. Designing Electrical Contacts to MoS_2 Monolayers: A Computational Study. *Phys. Rev. Lett.* **2012**, *108*, 156802. [CrossRef]
34. Buscema, M.; Barkelid, M.; Zwiller, V.; Van Der Zant, H.S.J.; Steele, G.A.; Castellanos-Gomez, A. Large and Tunable Photothermoelectric Effect in Single-Layer MoS_2. *Nano Lett.* **2013**, *13*, 358–363. [CrossRef] [PubMed]
35. Ghatak, S.; Pal, A.N.; Ghosh, A. Nature of Electronic States in Atomically Thin MoS_2 Field-Effect Transistors. *ACS Nano* **2011**, *5*, 7707–7712. [CrossRef] [PubMed]
36. Lee, E.; Lee, S.G.; Lee, W.H.; Lee, H.C.; Nguyen, N.N.; Yoo, M.S.; Cho, K. Direct CVD Growth of a Graphene/MoS_2 Heterostructure with Interfacial Bonding for Two-Dimensional Electronics. *Chem. Mater.* **2020**, *32*, 4544–4552. [CrossRef]
37. Fang, H.; Tosun, M.; Seol, G.; Chang, T.C.; Takei, K.; Guo, J.; Javey, A. Degenerate n-Doping of Few-Layer Transition Metal Dichalcogenides by Potassium. *Nano Lett.* **2013**, *13*, 1991–1995. [CrossRef] [PubMed]
38. Mak, K.F.; Shan, K.F.M.J. Photonics and optoelectronics of 2D semiconductor transition metal dichalcogenides. *Nat. Photon.* **2016**, *10*, 216–226. [CrossRef]
39. Yamamoto, M.; Wang, S.T.; Ni, M.; Lin, Y.-F.; Li, S.-L.; Aikawa, S.; Jian, W.-B.; Ueno, K.; Wakabayashi, K.; Tsukagoshi, K. Strong Enhancement of Raman Scattering from a Bulk-Inactive Vibrational Mode in Few-Layer $MoTe_2$. *ACS Nano* **2014**, *8*, 3895–3903. [CrossRef]
40. Goldstein, T.; Chen, S.-Y.; Tong, J.; Xiao, D.; Ramasubramaniam, A.; Yan, J. Raman scattering and anomalous Stokes–anti-Stokes ratio in $MoTe_2$ atomic layers. *Sci. Rep.* **2016**, *6*, 28024. [CrossRef] [PubMed]
41. Cho, H.; Kim, S.; Kim, S.; Zhao, J.H.; Seok, J.; Keum, J.; Baik, D.H.; Choe, J.; Chang, D.H.; Suenaga, K.J.; et al. Phase patterning for ohmic homojunction contact in $MoTe_2$. *Science* **2015**, *349*, 625–628. [CrossRef]
42. Zhou, L.; Xu, K.; Zubair, A.; Liao, A.D.; Fang, W.; Ouyang, F.; Lee, Y.-H.; Ueno, K.; Saito, R.; Palacios, T.; et al. Large-Area Synthesis of High-Quality Uniform Few-Layer $MoTe_2$. *J. Am. Chem. Soc.* **2015**, *137*, 11892–11895. [CrossRef]
43. Naylor, C.H.; Parkin, W.M.; Ping, J.; Gao, Z.; Zhou, Y.R.; Kim, Y.; Streller, F.; Carpick, R.W.; Rappe, A.M.; Drndić, M.; et al. Monolayer Single-Crystal 1T′-$MoTe_2$ Grown by Chemical Vapor Deposition Exhibits Weak Antilocalization Effect. *Nano Lett.* **2016**, *16*, 4297–4304. [CrossRef]
44. Li, H.; Tsai, C.; Koh, A.L.; Cai, L.; Contryman, A.W.; Fragapane, A.H.; Zhao, J.; Han, H.S.; Manoharan, H.C.; Abild-Pedersen, F.; et al. Activating and optimizing MoS_2 basal planes for hydrogen evolution through the formation of strained sulphur vacancies. *Nat. Mater.* **2016**, *15*, 364. [CrossRef] [PubMed]
45. Somvanshi, D.; Kallatt, S.; Venkatesh, C.; Nair, S.; Gupta, G.; Anthony, J.K.; Karmakar, D.; Majumdar, K. Nature of carrier injection in metal/2D-semiconductor interface and its implications for the limits of contact resistance. *Phys. Rev. B* **2017**, *96*, 205423–205433. [CrossRef]
46. Lu, Q.; Liu, Y.; Han, G.; Fang, C.; Shao, Y.; Zhang, J.; Hao, Y. Experimental investigation of the contact resistance of Graphene/MoS_2 interface treated with O_2 plasma. *Superlattices Microstruct.* **2018**, *114*, 421–427. [CrossRef]
47. Kappera, R.; Voiry, D.; Yalcin, S.E.; Branch, B.; Gupta, G.; Mohite, A.; Chhowalla, M. Phase-engineered low-resistance contacts for ultrathin MoS_2 transistors. *Nat. Mater.* **2014**, *13*, 1128–1134. [CrossRef] [PubMed]
48. Park, J.H.; Jung, E.H.; Jung, J.W.; Jo, W.H. A Fluorinated Phenylene Unit as a Building Block for High-Performance n-Type Semiconducting Polymer. *Adv. Mater.* **2013**, *25*, 2583–2588. [CrossRef]
49. Yu, L.; Lee, Y.-H.; Ling, X.; Santos, E.J.G.; Shin, Y.C.; Lin, Y.; Dubey, M.; Kaxiras, E.; Kong, J.; Wang, H.; et al. Graphene/MoS_2 Hybrid Technology for Large-Scale Two-Dimensional Electronics. *Nano Lett.* **2014**, *14*, 3055–3063. [CrossRef] [PubMed]
50. Das, S.; Appenzeller, J. Where Does the Current Flow in Two-Dimensional Layered Systems. *Nano Lett.* **2013**, *13*, 3396–3402. [CrossRef]
51. Kim, S.; Konar, A.; Hwang, W.-S.; Lee, J.H.; Lee, J.; Yang, J.; Jung, C.; Kim, H.; Yoo, J.-B.; Choi, J.-Y.; et al. High-mobility and low-power thin-film transistors based on multilayer MoS_2 crystals. *Nat. Commun.* **2012**, *3*, 1011. [CrossRef] [PubMed]